J Mater Sci: Mater Electron **(2026) 37:491**

Tailoring the microstructural and electromagnetic response of SPS-synthesized MgB_2 through organic $C_{15}H_{12}O_2$ additions

Asli Asiye Agil[1,*]

[1] *Faculty of Engineering, Department of Materials Science and Engineering, Hakkari University, 30000 Hakkari, Turkey*

Received: 17 December 2025
Accepted: 21 February 2026
Published online: 5 March 2026

© The Author(s), 2026

ABSTRACT

In this study, the microstructural, electrical, and electromagnetic properties of MgB_2 bulk superconductors modified with the organic additive of phenyl(3-phenyloxirane-2-yl)methane ($C_{15}H_{12}O_2$) were investigated. Pure and bulk MgB_2 samples doped with 0–20 wt% $C_{15}H_{12}O_2$ were produced by in situ Spark Plasma Sintering (SPS) at 850 °C, 50 MPa pressure, and 10 min. X-ray diffraction analyses showed that the hexagonal MgB_2 phase was predominantly preserved in all samples, with limited MgO formation observed at increasing addition rates. SEM analyses revealed that organic additive created controlled porosity and microstructural heterogeneity. Electrical measurements showed a limited decrease in the superconducting transition temperature and an increase in the normal-state resistivity in the doped samples. Magnetic characterization results revealed that the sample containing 15 wt% $C_{15}H_{12}O_2$ exhibited the highest critical current density and optimized pinning force at 20 K. Levitation force measurements performed under ZFC and FC conditions have shown a strong correlation between microstructure-derived pinning architecture and electromagnetic response. The results reveal that $C_{15}H_{12}O_2$ addition offers a suitable approach for effectively tuning the pinning and levitation properties of SPS-generated MgB_2 bulk superconductors.

1 Introduction

Since the discovery of MgB_2 with a superconducting transition temperature of approximately 39 K, it has become a significant candidate for bulk superconducting applications due to its simple crystal structure, low raw material cost, and superior electromagnetic performance at moderate cryogenic temperatures [1]. Bulk MgB_2 superconductors, in particular, stand out as promising materials for trapped field magnets, magnetic beds, and cryogenic levitation systems operating in the 20–30 K temperature range [2, 3].

The performance of bulk MgB_2 is determined by microstructural features such as density, grain bonding, secondary phase distribution, and defect architecture, and these parameters directly affect flux pinning efficiency and critical current density [4, 5]. Therefore, to overcome the porosity and weak grain cohesion frequently encountered in MgB_2 bulks produced by pressureless sintering, advanced densification techniques

Address correspondence to E-mail: asliasiyeagil@hakkari.edu.tr

https://doi.org/10.1007/s10854-026-16870-4

such as Spark Plasma Sintering (SPS), hot pressing (HP), hot isostatic pressing (HIP), and infiltration-growth (IG) have been widely investigated [6, 7]. Among these methods, SPS allows for the achievement of more refined microstructures and high phase purity at relatively low temperatures thanks to high heating rates, short sintering times, and simultaneous pressure-pulsed direct current application [8, 9]. However, simply increasing the density is often not enough to ensure optimum flux pinning, requiring precise microstructure engineering.

Carbon-based dopants are widely used to improve flux pinning in MgB_2; these dopants form pinning centers through mechanisms such as boron substitution, nano-scale secondary phase formation, and lattice disruptions [10, 11]. In recent years, organic compounds have gained increasing interest as alternative carbon sources due to their low decomposition temperatures, homogeneous distributions, and ability to form fine-scale defects during thermal decomposition [12, 13]. However, systematic studies on organically doped MgB_2 bulk superconductors synthesized by SPS, particularly those related to levitation force behavior, are limited.

In this context, this study comprehensively investigates the effects of phenyl(3-phenyloxirane-2-yl) methane ($C_{15}H_{12}O_2$) addition on the microstructural evolution, electrical transport properties, flux pinning behavior, and magnetic levitation performance of SPS-generated MgB_2 bulk superconductors. By considering density, phase composition, lattice parameters, microstructure, critical current density, pinning force scaling, and levitation characteristics together, the study reveals how organic additives shape the balance between densification and pinning, offering essential implications for the design of high-performance MgB_2 bulk materials.

Unlike conventional low-level carbon addition approaches, the present study deliberately employs a wide additive concentration range (0–20 wt%) in order to systematically investigate the competing effects of organic additive decomposition on densification, microstructural evolution, flux pinning efficiency, and electromagnetic response in bulk MgB_2. Such a broad composition window enables the identification of both the optimal performance regime and the over-addition limit, where excessive additive content leads to degradation of grain connectivity and superconducting coherence.

2 Experimental procedure

2.1 *Synthesis procedure of $C_{15}H_{12}O_2$–phenyl (3-phenyloxirane-2-yl) methanone*

The organic compound phenyl (3-phenyloxirane-2-yl) methanone ($C_{15}H_{12}O_2$) was synthesized by modifying a two-step method based on epoxidation and acylation reported in the literature. In the first step, the stilbene-derived aromatic precursor was reacted via peracetic oxidation to form an epoxide ring. The resulting epoxide intermediate was then subjected to an acylation reaction with benzoyl chloride. The two-step synthesis route employed in this study is a modified procedure adapted from well-established organic synthesis strategies for epoxide-containing aromatic ketone derivatives reported in the literature [14]. The synthesis protocol includes the following steps:

i. The aromatic precursor was dissolved in an ethanol medium and peracetic acid was added to the mixture in a controlled manner.
ii. The reaction continued for 4–6 h at room temperature, yielding an epoxide intermediate.
iii. This intermediate product was reacted with benzoyl chloride in dichloromethane, and acylation was completed under basic conditions (triethylamine).
iv. The solution was purified and precipitated, and the crystalline product was dried under vacuum.

In this way, a high-purity additive material was obtained through a completely controlled organic synthesis. Phase purity was assessed by XRD analysis, which showed no detectable secondary crystalline phases within the resolution limits of the technique.

2.2 *Fabrication of MgB_2–$C_{15}H_{12}O_2$ bulk superconductors by SPS*

The MgB_2-based bulk samples produced in this study were labeled S0, S5, S10, S15, and S20 according to their additive ratios. Mg (Alfa Aesar, − 325 mesh, 99.8%), nano-sized boron powder (Pavesium) with a stated purity in the range of 99 + to 99.999% (as specified by the supplier) was used as the boron source, and the synthesized organic additive $C_{15}H_{12}O_2$ were used as starting powders. Additive ratios were determined as 0, 5, 10, 15, and 20 wt%, respectively,

and the required amount of Mg, B, and additives for each sample was weighed and prepared.

The weighed powder mixtures were mixed for 5 h at 150 rpm in a Retsch PM400 ball mill using a tungsten carbide jar and balls to ensure homogeneity. Ball milling was performed using a ball-to-powder weight ratio of 10:1, and no inert gas was introduced into the milling jar prior to the process. The powders obtained at the end of the mixing process were placed in graphite molds of 20 mm diameter and each sample was processed under the same sintering conditions.

The sintering process was carried out in an HPD-50 (FCT Systeme GmbH, Germany) model Spark Plasma Sintering device at 850 °C, 50 MPa uniaxial pressure, and a 10-min holding time. These production parameters were chosen based on the previous work of our research group, which determined the optimum MgB_2 sintering parameters [15].

After sintering was completed, the samples were removed from the mold, the surface graphite residue was sanded clean, and they were prepared to size for characterization tests. By this method, MgB_2–$C_{15}H_{12}O_2$ bulk superconductors codenamed S0 (pure), S5, S10, S15, and S20, corresponding to 0, 5, 10, 15, and 20 wt% $C_{15}H_{12}O_2$ additive, respectively, were successfully produced.

2.3 Characterization techniques

The produced MgB_2–$C_{15}H_{12}O_2$ bulk superconductor samples were characterized using various structural, microstructural, magnetic, and electrical analysis techniques. The relative densities of the samples were determined using Archimedes' principle by dividing the measured actual density values by the theoretical density of MgB_2. Phase analysis was carried out under CuKα radiation using a Rigaku Miniflex X-ray diffraction (XRD) device to examine the crystal structure and phase components formed after sintering.

Scanning electron microscopy (SEM) analyses were performed using a Thermo Fisher Scientific Phenom XL G3 Desktop SEM to evaluate the microstructure, grain morphology, and additive distribution of the samples. To assess superconductivity behavior, magnetic and transport characterizations were performed using the PPMS–CFMS 12 T (Cryogenics) system. In transport measurements, resistance–temperature (ρ–T) analyses based on four-point contact were taken, and in magnetic characterizations, M–H curves and field-dependent critical current density were evaluated.

Levitation characterizations were performed based on the method described in detail in our research group's studies of pure MgB_2 bulk superconductors synthesized using the SPS method at various temperatures [15]. Measurements were made using a custom-designed levitation measurement setup integrated into the PPMS cryogenic system, and the magnetic levitation force was recorded as temperature and distance-dependent.

3 Results and discussion

This section comprehensively evaluates the structural, microstructural, and electromagnetic properties of pure and $C_{15}H_{12}O_2$-doped MgB_2 bulk superconductors produced by the SPS method. First, relative densities determined by Archimedes' principle are presented, followed by an examination of XRD patterns and lattice parameters derived from these patterns. The morphological characteristics of the samples were evaluated via SEM images; the superconductivity behavior was discussed through resistivity–temperature measurements, levitation force analyses, and magnetization (M–H) curves obtained in a PPMS medium. The effect of the dopant material on flux pinning mechanisms was analyzed in detail by calculating the magnetic field-dependent critical current density (J_c) and pinning force (F_p).

3.1 Densification behavior and relative density

According to the Archimedes' results given in Fig. 1, the relative density of the pure sample S0 is approximately 83–84%, while the density values in the organically doped S5–S20 samples are in the range of 77–79%, showing a slight decrease with the addition of the dopant. This decrease can be attributed to the fact that the $C_{15}H_{12}O_2$ additive decomposes during the SPS process to form a gas phase, and this, combined with the volatility of Mg, increases pore formation. A similar phenomenon has been observed in organometallic $Ge_2C_6H_{10}O_7$-doped SPS-MgB_2 samples, associated with vacuum/ripple signals accompanying the decomposition of the dopant [16].

The relatively lower densities observed for the doped samples (77–79%) indicate an increased level of residual porosity, which may adversely affect

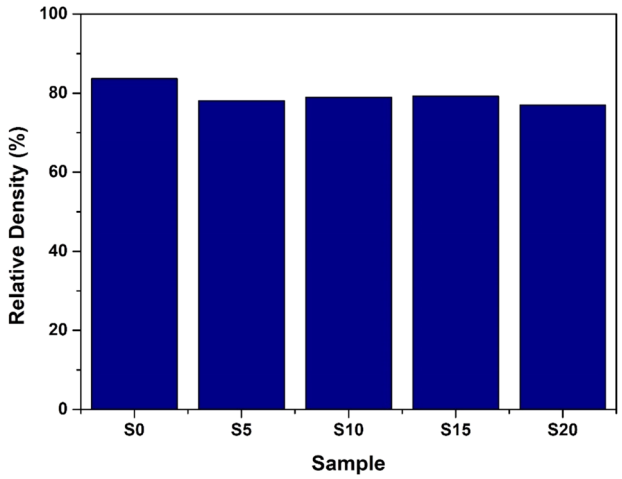


Fig. 1 Relative densities of MgB_2–$C_{15}H_{12}O_2$ samples (S0–S20)

long-term mechanical integrity, including strength, fracture resistance, and durability under cyclic or vibrational loading. Such porosity could limit the applicability of these materials in mechanically demanding trapped-field magnet systems or large-scale engineering components. However, it should be noted that the present work primarily focuses on tailoring electromagnetic performance rather than maximizing structural robustness. In this context, moderately porous MgB_2 bulks remain highly relevant for applications such as magnetic levitation, laboratory-scale demonstrators, and cryogenic magnetic devices, where mechanical stresses are relatively low and flux pinning efficiency is the dominant performance criterion. In comparison, higher-density SPS or HIP-processed MgB_2 bulks reported in the literature are more suitable for large-scale and mechanically robust applications, while the present materials provide valuable insight into the trade-off between densification, pinning architecture, and electromagnetic response.

Most bulk MgB_2 materials produced by the SPS method in the literature have been reported to have high relative densities (90–97% and above). For instance, it has been reported that > 93% relative density is achieved with SPS in GeO_2-doped MgB_2 [9], while in organometallic-doped ex-situ SPS samples, the relative density is generally above 90% [16]. Kang et al. obtained MgB_2 with approximately 97% relative density using SPS around 1150 °C [17], while the review study by Zhang et al. shows that MgB_2 bulks prepared with SPS can approach the theoretical density quite closely under appropriate temperature/pressure combinations [18]. In ultra-high-pressure field-assisted sintering studies, values very close to the theoretical density at the 3 GPa level are reported, while in conventional SPS, the relative density at 100 MPa pressure remains around 90% [19]. Ağıl et al. showed that the density of MgB_2 bulk synthesized by in situ SPS at different temperatures increased with sintering temperature, with the highest density at 900 °C and optimum equilibrium in terms of phase formation at 850 °C [15]. In this context, the preference for relatively mild sintering conditions, such as 850 °C/50 MPa and a 20-mm-diameter disk geometry in the present study, when evaluated together with the decomposition of the organic phase in the doped samples, explains why the relative densities remain slightly lower than those of classical "high-density SPS-MgB_2" samples.

Compared to methods other than SPS, the obtained relative density values in the range of 77–84% are modest, especially for doped samples, but are at a competitive level when compared to conventional pressureless sintered MgB_2 bulks. In the studies by Zhao et al. and Arvapalli et al., it is emphasized that MgB_2 bulks obtained by conventional solid-state sintering at ambient pressure exhibit low density and weak grain-to-grain cohesion, thus limiting critical current densities [20, 21]. Densities of MgB_2 discs produced by hot pressing under pressures of 50–60 MPa are generally reported to be in the range of 85–91%. For example, Durrell et al. achieved values around 91% of the theoretical density with uniaxial hot pressing and obtained a trapped area of over 3 T with these samples [2, 22]. In bulk MgB_2 subjected to hot isostatic pressing (HIP), it has been reported that both density and grain cohesion are significantly improved due to isostatic pressure, and microwave and magnetic performance increase accordingly [23]. On the other hand, it has been shown that bulk MgB_2 materials produced by infiltration-growth techniques achieve absolute density values of approximately 2.4 g/cm^3 (approximately 90% of the theoretical value), and this is directly related to high J_c and trapped field performance [3]. Finally, next-generation studies combining L-PBF (laser powder bed fusion) with SPS and numerical modeling studies comparing HIP/SPS/infiltration methods reveal that volumetric density is very sensitive to the production technique; high-pressure methods like SPS and HIP provide a significant advantage over traditional pressureless sintering [7, 24].

In this general context, the higher density of the S0 sample in the present study compared to the others indicates that the undoped MgB_2 phase can densify more effectively under SPS; while in the $C_{15}H_{12}O_2$-doped S5–S20 samples, the gas phases released as a result of addition decomposition and possible second phase formations slightly increase porosity. However, the fact that the relative densities of all samples are close to each other suggests that the addition does not completely suppress densification, but instead acts as a parameter adjusting the microstructure and flux pinning mechanisms. Therefore, in the following subsections, the effects of this limited variation observed in density on the superconducting transition temperature, critical current density, and levitation performance will be examined separately.

3.2 Phase analysis and lattice parameters

When the XRD patterns given in Fig. 2 are examined, it is seen that the main phase in all samples is MgB_2, exhibiting a hexagonal AlB_2-type structure. The diffraction peaks corresponding to the MgB_2 phase were identified using the standard ICDD PDF-2#65-3383. In addition, weak MgO peaks appear, especially at high dopant ratios. The presence of the MgO phase is associated with the inevitable reaction of Mg with oxygen during processing. Similarly, the secondary MgO phase has been observed alongside the main MgB_2 phase in other bulk studies of MgB_2 produced by SPS [8]. The increased prominence of MgO, particularly in the S20 sample, can be attributed both to the increased amount of additive facilitating Mg evaporation/oxidation and to the formation of intermediate species that carry oxygen into the environment during the decomposition of the organic $C_{15}H_{12}O_2$ additive. In methods other than SPS (traditional pressureless sintering, hot press, HIP, infiltration, etc.), most studies report that phases such as MgO and MgB_4 are formed in higher proportions alongside MgB_2, and even the Mg phase is clearly detected by XRD in pressureless sintered or incompletely reacted samples [25–27]. From this perspective, the fact that the patterns obtained with SPS in the present study essentially exhibit single-phase MgB_2 characteristics indicates a very positive situation in terms of phase purity, even if the density values are below the theoretical density.

The lattice parameters of pure MgB_2 reported in the literature are generally given as $a \approx 3.086$ Å and $c \approx 3.524$ Å [28]. The lattice parameters calculated in this study are summarized in Table 1. For the S0 sample, values of $a = 3.08$ Å and $c = 3.52$ Å were obtained, while for the doped samples, values in the range of

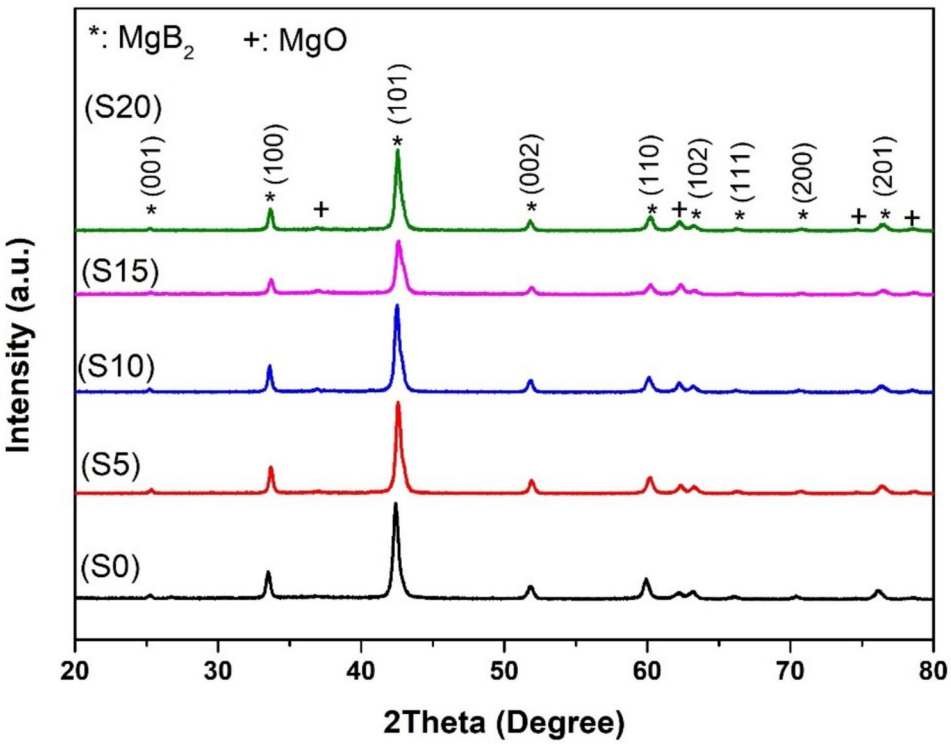


Fig. 2 XRD patterns of SPS-synthesized MgB_2–$C_{15}H_{12}O_2$ samples (S0–S20)

Table 1 Lattice parameters obtained from XRD data of MgB_2 samples with different $C_{15}H_{12}O_2$ addition ratios

Sample	a (Å)	c (Å)
S0	3.08	3.52
S5	3.07	3.52
S10	3.08	3.53
S15	3.07	3.53
S20	3.07	3.53

a = 3.07–3.08 Å and *c* = 3.52–3.53 Å were obtained. These values both confirm that the crystal structure is the targeted hexagonal MgB_2 phase and demonstrate that the organic addition affects the crystal lattice only to a limited extent. A noteworthy point is the observation of a slight decrease in the *a*-parameter (3.08 → 3.07 Å) and a minimal increase in the *c*-parameter (3.52 → 3.53 Å) with the addition of carbon. This behavior is consistent with the "*a*-axis reduction, *c*-axis negligible or slight increase" trend reported in the literature for $Mg(B_{1-x}C_x)_2$ systems, where carbon is incorporated by substitution into boron layers. These studies show that with increasing C content, the *a*-parameter decreases almost linearly, while the *c*-parameter remains constant mainly or increases only slightly [10, 29–31]. This similarity suggests that the $C_{15}H_{12}O_2$ contribution may dissociate during SPS, resulting in at least a portion of it undergoing partial C precipitation/displacement in the MgB_2 lattice. The absence of a discrete carbonic phase in the XRD also provides further evidence that this form is amorphous, mainly or nano-sized. The lattice parameters were calculated from the XRD peak positions of the (100), (002), and (101) reflections using Bragg's law and the hexagonal lattice relations. The reported values are limited to two decimal places, consistent with the instrumental resolution and peak fitting accuracy of the laboratory XRD system.

When compared with reported lattice parameters from different production methods, the values in the present study are in good agreement with bulk MgB_2 produced by both SPS and other densification techniques. For example, values of around *a* ≈ 3.080 Å and *c* ≈ 3.46 Å have been reported for MgB_2 discs produced by hot pressing at 1000 °C [32]. It has been reported that in bulk samples produced in situ or ex situ by SPS, the lattice parameters generally converge to values of around 3.08 Å for *a* and around 3.52–3.53 Å for *c* [8]. Similar lattice parameters for the primary phase MgB_2 have been reported in high-density MgB_2 bulk materials obtained by the infiltration-growth (IG) method. Additionally, the Mg and intermediate boride phases formed in the process have been detected by XRD [3, 33]. Therefore, the lattice parameters obtained in this study are highly consistent with the "typical" structural range of MgB_2 bulk materials prepared by different production techniques, indicating that $C_{15}H_{12}O_2$ addition does not cause significant distortion in the MgB_2 lattice, but rather affects it through fine-scale lattice distortions and secondary phase formation. It should be emphasized that the inference of partial carbon substitution in the present study is based on indirect evidence, namely lattice parameter variations observed by XRD, rather than direct compositional analysis. Direct confirmation of carbon substitution would require dedicated compositional or spectroscopic analyses such as EDS, elemental mapping, or other advanced techniques, which are beyond the scope of the present work.

When evaluated together with the density results, the fact that the S0 sample has both the highest relative density and the lowest amount of secondary phase in the XRD pattern indicates that undoped MgB_2 exhibits more effective crystal growth and grain-to-grain bonding under SPS. In $C_{15}H_{12}O_2$-doped S5–S20 samples, considering the limited decrease in relative density observed together with the slight increase in MgO observed in XRD, it can be concluded that the addition increases microporosity and secondary phase content somewhat rather than completely suppressing densification, while preserving the MgB_2 main lattice. It has been reported in the literature that nano/submicron second phases such as MgO, MgB_4, and similar phases can function as effective flux pinning centers in high fields when properly distributed [9, 16]. Therefore, the $J_c(H)$ and pinning force results to be presented in the following sections will be critical to revealing the actual effect of this phase evolution, determined by XRD, on superconducting and levitation performance.

3.3 Microstructure analysis (SEM)

Secondary electron SEM images obtained at the same magnification (see Fig. 3) show that the undoped S0 sample exhibits a relatively more compact microstructure, while the doped samples (S5–S20) show a distinctly porous microstructure. In the S0 sample, dense, well-connected MgB_2 grains in the form of convoluted lamellae are observed, while in the doped samples, larger and often interconnected pores appear

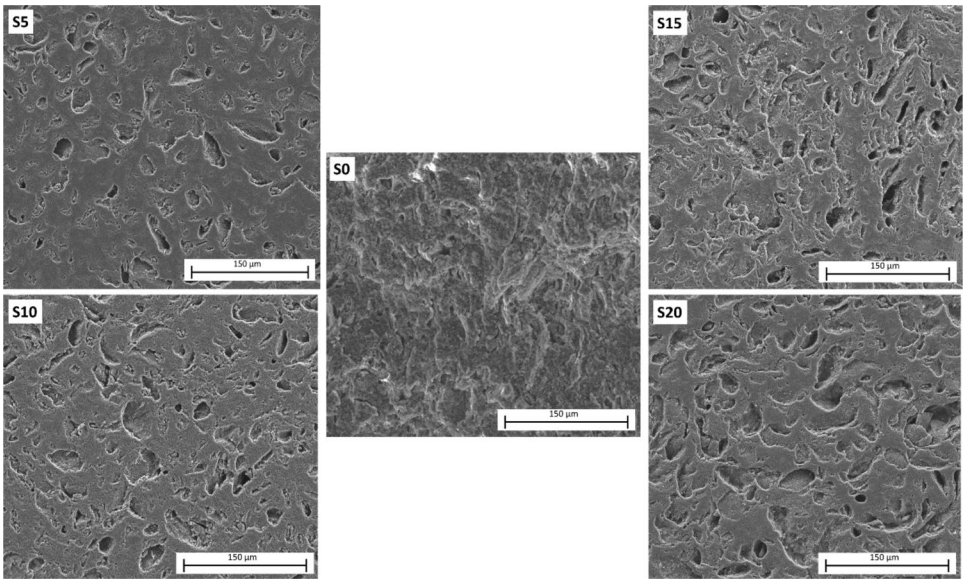


Fig. 3 SEM surface morphologies of MgB_2–$C_{15}H_{12}O_2$ samples (S0–S20)

with increasing addition ratio. This situation is consistent with the relative density results discussed in the previous section. The fact that sample S0 has the highest relative density and the density decreases slightly in samples S5–S20 is directly related to this additional porosity seen in SEM. It can be assumed that volatile species formed by the decomposition of organic $C_{15}H_{12}O_2$ during SPS and Mg evaporation feed the pores, and that the MgO phase detected in XRD, especially at high addition ratios, is a result of this decomposition/oxidation process. In previous studies on MgB_2 bulk synthesized by SPS at different temperatures, it was reported that porosity decreased. Intergranular bonding strengthened as the sintering temperature increased, and it was shown that the most suitable microstructure and superconductivity properties were obtained around 850–900 °C [15].

In the literature, dense MgB_2 bulk samples produced by SPS are reported to have a tightly packed structure consisting of nano-submicron-sized grains, along with finely dispersed secondary phases containing MgO and high magnesium boride (MgB_{4-6}) in places. These studies show that a nearly pore-free microstructure and consequently high grain cohesion can be obtained at high pressures (≈ 50–100 MPa) and optimized temperatures [34]. In contrast, it is emphasized that SEM images of MgB_2 bulk samples sintered under pressure in a conventional solid-state or Ar atmosphere show high porosity and relatively loosely packed grains similar to S5–S20 samples, thus limiting relative density and electrical coupling [35]. In hot pressing and especially high-pressure sintering (1–2 GPa) studies, it has been reported that the amount of porosity is significantly reduced, intergranular boundaries are tightened, and consequently, the critical current density is increased dramatically [34, 36]. In C-doped MgB_2 bulk samples produced by the infiltration-growth (IG) method, an almost poreless, fully dense microstructure and consequently very high trapped field values have been reported [5]. This comparison shows that the microstructure of the organic-modified SPS samples in the present study is more porous than the "fully dense" samples of classical SPS; however, it exhibits a more stable density–porosity profile compared to pressureless sintering and some solid-state reaction samples.

With increasing $C_{15}H_{12}O_2$ ratio, the morphology of the pores observed in S5–S20 samples also changes, and larger, locally oriented, and interconnected voids become dominant. It is known that such porous structures can, on the one hand, limit electrical coupling by reducing the effective cross-sectional area, and on the other hand, as emphasized in the literature, can function as defect/void-based flux pinning centers that hinder vortex movement [4, 12, 21]. In high-performance bulk studies of MgB_2, it has been shown that the fine-grained microstructure formed by nano-submicron grains, along with microporosity and dispersed secondary phases, contributes to firm grain boundary pinning and high J_c values [35, 37]. In this context, the S0 sample can provide lower grain boundary resistance and good carrier pathways at low fields due

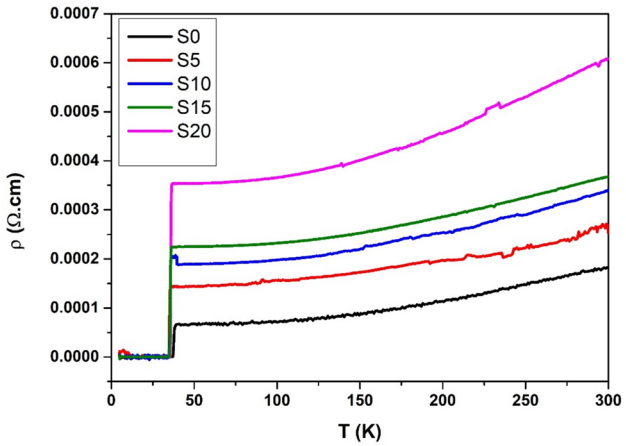


Fig. 4 Resistivity–temperature (ρ–T) curves of MgB_2–$C_{15}H_{12}O_2$ samples (S0–S20)

Table 2 Superconducting transition temperatures ($T_{c,onset}$, $T_{c,zero}$), transition width (ΔT_c), and RRR values obtained from resistivity–temperature measurements of S0–S20 samples

Sample	$T_{c,onset}$ (K)	$T_{c,zero}$ (K)	ΔT_c (K)	RRR
S0	38.99	37.80	1.19	2.72
S5	35.27	34.83	0.44	1.83
S10	36.02	34.53	1.49	1.80
S15	36.47	34.52	1.95	1.63
S20	36.02	35.27	0.75	1.72

to better grain coupling. In contrast, pores in doped samples, together with second phases such as MgO determined by XRD, can act as effective pinning centers, especially at high magnetic fields. This hypothesis, when evaluated together with the resistivity–temperature, M–H, $J_c(H)$, and pinning force results to be presented in later sections, will reveal that $C_{15}H_{12}O_2$ addition is a critical parameter that reconfigures the MgB_2 microstructure not only in terms of density but also in terms of flux dynamics and levitation properties.

3.4 Resistivity-temperature behavior and superconducting transition properties

The ρ–T curves given in Fig. 4 show that all samples exhibit metallic behavior in the normal region and undergo a superconducting transition around 39 K. According to Table 2, for the pure S0 sample, $T_{c,onset}$ = 38.99 K, $T_{c,zero}$ = 37.80 K, transition width ΔT_c = 1.19 K, and RRR = 2.72; while in $C_{15}H_{12}O_2$-doped samples, $T_{c,onset}$ decreases to 35.27–36.47 K, $T_{c,zero}$ to 34.52–35.27 K, ΔT_c to 0.44–1.95 K, and RRR to 1.63–1.83. These results show that the additive increased both intragranular scattering (C substitution, secondary phases such as MgO) and intergranular scattering (porosity, grain boundary oxides), and that the carriers traveled through a more "dispersive" transport network, consistent with the relative density decrease and increased porosity observed in previous density and SEM analyses.

In the literature, $T_c \approx$ 39–39.5 K and RRR ≈ 2–3 in polycrystalline samples are considered typical for high-density SPS-MgB_2 bulks. For instance, Xing et al. reported ρ(300 K) ≈ 43.8 $\mu\Omega$·cm, ρ(40 K) ≈ 17.1 $\mu\Omega$·cm, and RRR = 2.56 in their study, where they condensed nanostructured MgB_2 bulks with SPS, and emphasized that this is quite close to other polycrystalline MgB_2 bulks [4]. A recent review of MgB_2 bulk technology also states that RRR values in samples produced by methods such as SPS, hot press, and HIP are mainly in the 2–3 range, and that this range is characteristic of "well-coupled" polycrystalline MgB_2 [38]. In this context, the RRR value of sample S0 = 2.72, when evaluated together with the high phase purity XRD pattern and more compact SEM microstructure, indicates a strong electrical coupling that is highly compatible with well-sintered SPS-MgB_2 bulk materials.

It has been reported that in HIP-MgB_2 bulk samples densified at higher pressures, porosity is further reduced, resulting in a decrease in room temperature resistivity and a RRR generally around 3–3.5. Gajda et al. showed that the increased density and improved microstructure after HIP significantly increased the critical parameters [39]. Studies comparing the trapping field performance of bulk MgB_2 produced by HIP and infiltration-growth (IG) methods also show that almost entirely dense (> 2.3–2.4 g cm^{-3}) samples can be obtained with these methods [3, 7]. In contrast, MgB_2 bulks produced by conventional solid-state (pressureless) sintering exhibit higher resistivity, wider T_c transitions, and generally RRR ≤ 1.5 values, which are associated with lower relative density and weak grain coupling [40, 41]. This comparison reveals that the S0 sample exhibits a significantly superior electrical coupling compared to pressureless sintering, while remaining relatively close to typical SPS/HIP bulks.

The suppression of T_c by several Kelvin and the reduction of RRR to the 1.6–1.8 range in $C_{15}H_{12}O_2$-doped S5–S20 samples are very consistent

with the literature on MgB_2 doped with organic carbon sources. Vajpayee et al. showed that in bulk MgB_2 doped with adipic acid ($C_6H_{10}O_4$), C replaces B, resulting in a decrease in T_c from 38.4 to 34.9 K and a reduction in the *a*-parameter [42]. Similarly, studies of MgB_2 doped with sucrose ($C_{12}H_{22}O_{11}$) and other carbonaceous chemical additives have reported that the normal region resistivity is increased, the RRR is decreased, and T_c is suppressed by several Kelvin; however, H_{c2} and J_c are significantly improved, especially at high magnetic fields [11]. Studies examining the addition effect using statistical models also emphasize that room temperature resistivity and RRR become significant scattering indices due to the disruption of the MgB_2 lattice [13]. Although resistivity-based connectivity models such as that proposed by Rowell can provide quantitative estimates of the effective current-carrying area, their direct application to organically modified SPS-processed MgB_2 bulks is nontrivial due to the simultaneous influence of disorder, secondary phases, and porosity.

3.5 Magnetic hysteresis, critical current density, and pinning behavior

The *M–H* curves measured at 20 K, given in Fig. 5(a), show significant differences in magnetic hysteresis width depending on the addition ratio. The fact that sample S15 exhibits the widest hysteresis loop indicates that the effective pinning centers limiting vortex movement are stronger in this sample. In the Bean critical-state model, the critical current density J_c is directly proportional to the magnetic moment difference ΔM, so this broadening of the *M–H* curves is directly reflected in the J_c–*H* behavior. In this study, the critical current density from magnetic measurements was calculated based on Bean's critical-state model [43, 44]. The expression $J_c = 20\ \Delta M/[a(1 - a/3b)]$ used for rectangular cross-section samples is widely applied within the scope of the extended Bean approach [45].

The 20 K J_c–*H* curves presented in Fig. 5(b) show that sample S15 reaches the highest J_c values at low magnetic fields, followed by sample S5, while samples S10, S0, and S20 remain at lower J_c levels. This ranking, when evaluated together with previous density, XRD, and SEM analyses, reveals that not only

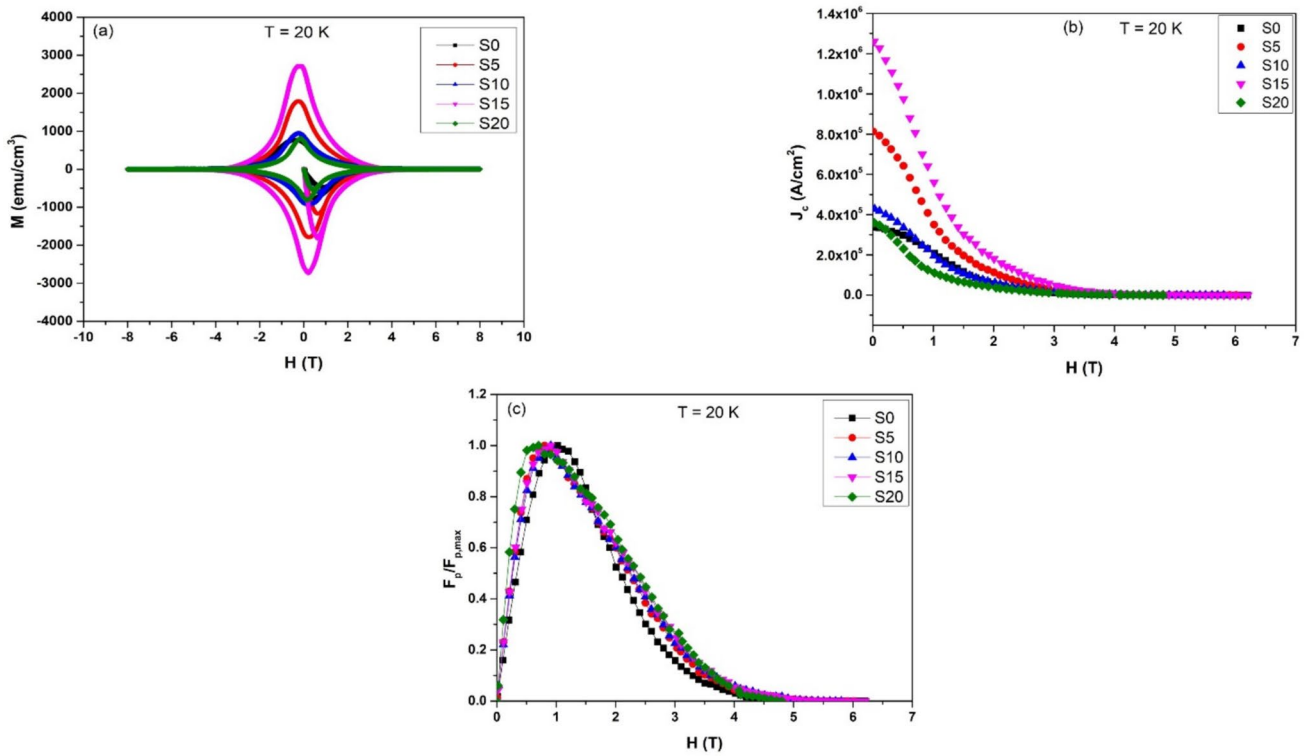


Fig. 5 **a** *M–H* hysteresis loops at 20 K, **b** J_c–*H* curves from the Bean model, and **c** normalized pinning force versus magnetic field

densification but also the microstructural pinning architecture plays a decisive role. The MgO secondary phases observed in XRD analyses, the fine-scale heterogeneity and pore structure that developed with the addition in SEM images, and the small changes detected in lattice parameters may have created a suitable defect spectrum, particularly in sample S15, which strengthens the vortex pinning. In MgB_2 bulk superconductors containing carbon-based dopants, it has been widely reported in the literature that $J_c(H)$ performance improves despite a limited decrease in T_c [4, 5].

When compared in terms of production method, it is known that in bulk MgB_2 superconductors produced by SPS, although high density is obtained, J_c can decrease rapidly with field; however, the high field performance can be significantly improved by creating suitable defects and addition. Studies that examine the J_c–microstructure relationship in SPS-concentrated MgB_2 bulks show that this method offers an advantage, especially in terms of the formation of nano-scale pinning centers [4]. In contrast, MgB_2 bulk produced by methods such as hot pressing, HIP, and infiltration-growth (IG) has been reported to exhibit particularly application-oriented performances (e.g., trapped field) due to higher densification and strong grain cohesion. Classical studies addressing the relationship between critical current density and trapped area in large-diameter MgB_2 disks produced by the hot-press method clearly demonstrate this situation [2, 7].

The normalized pinning force $(F_p/F_{p,max})$–H curves given in Fig. 5(c) show the presence of a single dominant pinning peak in all samples and reveal that the peak locations are clustered in the mid-magnetic field region. Such scaled pinning analyses are often considered in conjunction with the Kramer–Dew-Hughes approach to assess the character of the vortex pinning mechanism [46]. Current studies on the interpretation of normalized pinning force curves in MgB_2 bulk superconductors show that complex pinning mechanisms involving both nano-sized second phases and grain boundary pinning are standard [47].

In this context, both the superior performance of the S15 sample in the J_c–H curve and the shape of the $F_p/F_{p,max}$ curve suggest that the distribution and efficiency of the pinning centers in this sample are approaching a more optimized combination. In contrast, the decrease in J_c values in the S20 sample despite the increasing addition ratio indicates that the mechanism of "excessive addition → increased porosity and weakening of grain connection → decrease in effective flow carrying cross-section," as frequently reported in the literature, has become dominant [5]. The inclusion of the 20 wt% $C_{15}H_{12}O_2$ sample therefore serves as an intentional upper-bound reference, clearly illustrating the transition from beneficial pinning enhancement to connectivity-dominated performance degradation.

In conclusion, when Fig. 5(a–c) is considered together, it is understood that the S15 sample with 15 wt% $C_{15}H_{12}O_2$ addition broadens magnetic hysteresis, increases the field-dependent critical current density, and significantly improves the vortex pinning behavior while maintaining the limited suppression in T_c at an acceptable level. These results are consistent with the previously discussed density, XRD, SEM, and electrical characterization findings, demonstrating that $C_{15}H_{12}O_2$ addition creates an optimal pinning architecture in MgB_2 bulk superconductors.

3.6 Levitation and guiding force behavior

It should be noted that all levitation force measurements were performed on bulk samples with identical geometry and nominal dimensions, fabricated using the same 20-mm graphite die. Therefore, direct comparison of absolute levitation force values provides a meaningful quantitative assessment of electromagnetic performance, and additional normalization by sample volume or mass would not affect the relative trends observed in this study. The levitation measurements were carried out under identical experimental conditions using the same force sensor, magnet configuration, and approach protocol. Although a formal statistical uncertainty analysis was not conducted, the observed force–distance trends were reproducible across repeated measurements, with the primary sources of uncertainty arising from positioning accuracy and sensor resolution.

The F_x (guidance/lateral force)–x curves in FC mode given in Fig. 6(a, b) show that the lateral magnetic stability (restoring force) behavior of the samples is sensitive to both the addition ratio and temperature. At 20 K (Fig. 6(a)), the curves are "smoother" and have higher amplitudes, while at 25 K (Fig. 6(b)), the amplitudes generally decrease, and some samples show increased hysteresis behavior. This situation is consistent with the weakening of the lateral guiding

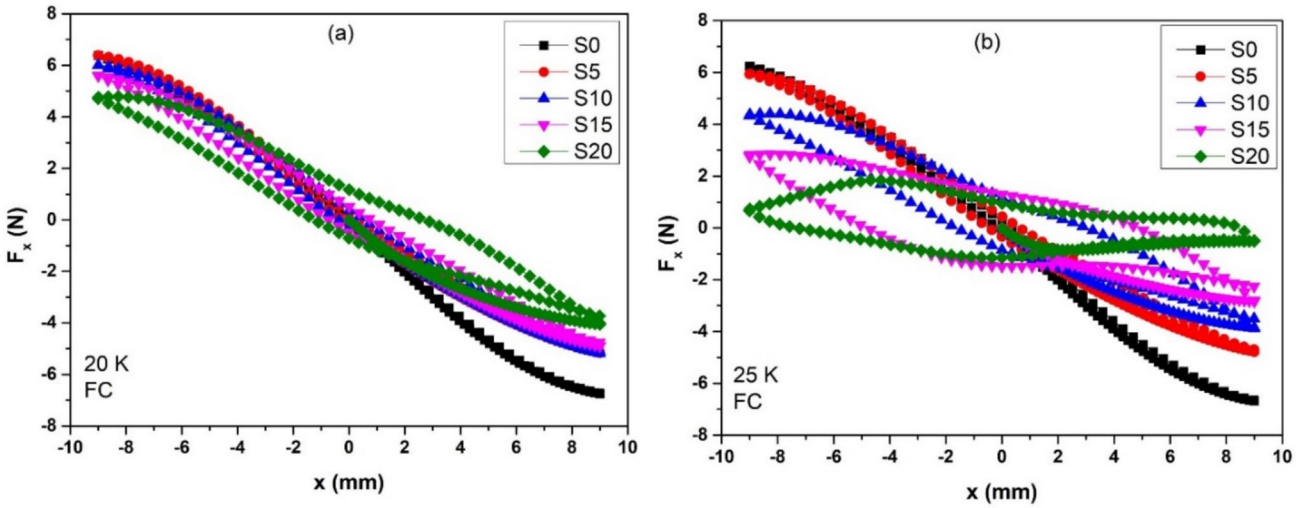


Fig. 6 Lateral (guiding) force (F_x–x) behavior of MgB_2–$C_{15}H_{12}O_2$ bulk superconductors measured in FC mode at **a** 20 K and **b** 25 K

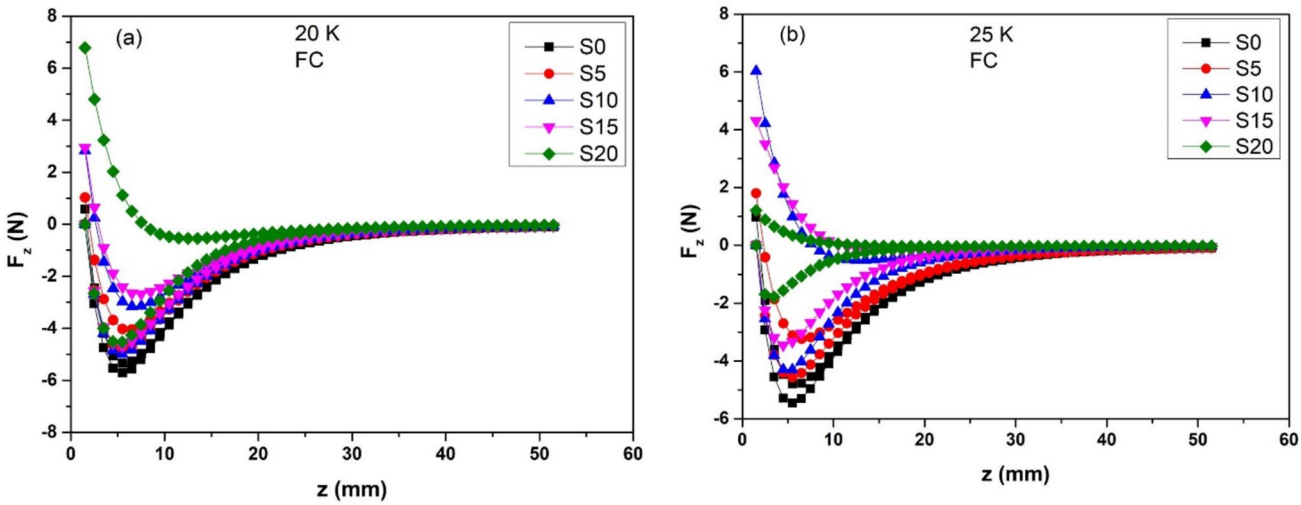


Fig. 7 Vertical levitation force (F_z–z) behavior of MgB_2–$C_{15}H_{12}O_2$ bulk superconductors measured in FC mode at **a** 20 K and **b** 25 K

force due to the decrease in critical current density with increasing temperature. It has been reported in the literature that lateral (guidance) force in MgB_2 bulks is observed under FC conditions, and that additive/treatment conditions can significantly alter the F_x behavior [48].

The F_z (vertical levitation force)–z curves in FC mode presented in Fig. 7(a, b) reveal that the force increases rapidly as the z distance decreases in all samples. After reaching maximum/minimum values in a particular region, it is damped by z. In the FC regime, it is expected that both repulsive and attractive components can be seen together due to the trapped flux within the superconductor, and the curves will have a more complex/hysteretic form. This behavior is a typical characteristic reported under FC conditions in levitation force measurements for maglev applications of MgB_2 bulks [49, 50].

In contrast, in the ZFC mode given in Fig. 8(a, b), it is noteworthy that the repulsive forces are significantly higher in the F_z–z curves, especially at small z distances. In the ZFC regime, since the sample is cooled in the absence of a magnetic field, the Meissner effect and strong shielding currents become more dominant when it is brought closer to a permanent magnet. Therefore, the initial repulsive force is

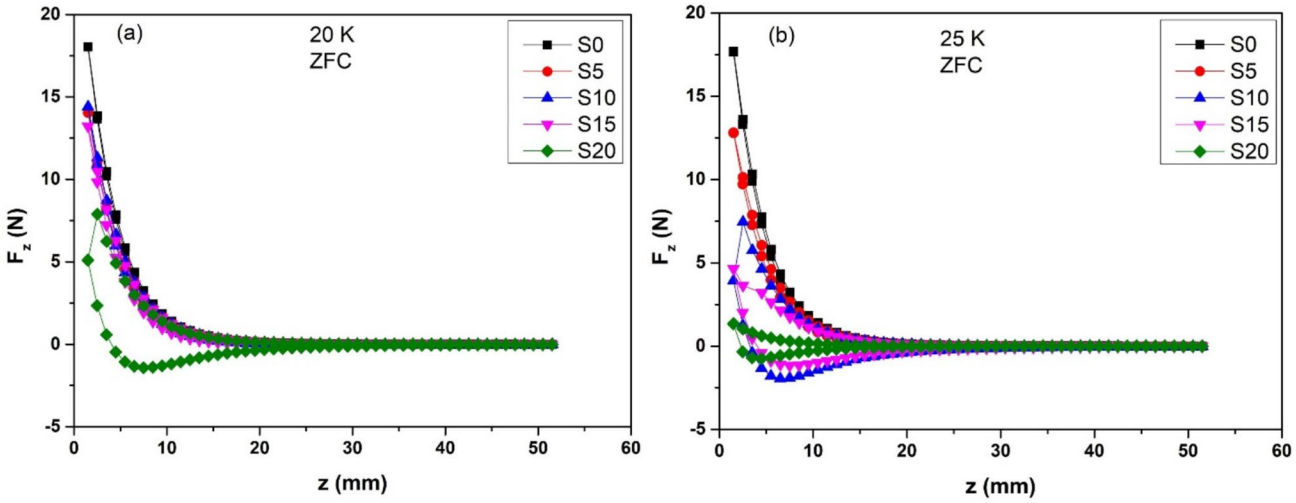


Fig. 8 Vertical levitation force (F_z–z) behavior of MgB_2–$C_{15}H_{12}O_2$ bulk superconductors measured in ZFC mode at **a** 20 K and **b** 25 K

expected to increase compared to FC. This "ZFC > FC" trend is very commonly reported in the MgB_2 bulk levitation literature [51]. In our case, increasing from 20 to 25 K (Fig. 8(a, b)) is consistent with the general decrease in ZFC repulsive forces, the reduction in J_c with increasing temperature, and the weakening of the effective shielding current.

The differences between samples fit well with the density–microstructure–pinning balance discussed in previous sections. In the ZFC regime, high repulsive forces generally indicate better grain connection/connectivity and more effective shielding currents, while in the FC regime, the shape and hysteresis of the force are more related to flux trapped capacity and pinning architecture. Therefore, a sample showing stronger pinning/$J_c(H)$ in magnetic measurements (e.g., composition prominent in 20 K magnetic analyses) can be expected to show an advantage in levitation measurements, especially under FC conditions. However, as the dopant increases, the net levitation performance may be limited if the density/connection loss becomes more pronounced. In MgB_2 bulk samples, this "pinning increase ↔ linkage loss" balance is frequently emphasized in samples produced by methods such as SPS and HP/HIP [38]. Furthermore, the study by Durrell et al. can be given as a classic reference, showing that the high trapped field performance obtained in large disks produced with HP is based on the link/pinning balance [2].

4 Conclusion

In this study, pure and $C_{15}H_{12}O_2$-doped MgB_2 bulk superconductors were successfully produced by in situ Spark Plasma Sintering at 850 °C and 50 MPa pressure. Structural analyses showed that the hexagonal MgB_2 phase was predominantly preserved in all samples, with limited secondary phase formation and increased microstructural heterogeneity with increasing addition rates. Although the organic additive partially reduced the relative density, it significantly affected the magnetic performance by creating a defect architecture favorable for flux pinning. Electrical measurements revealed that the addition of doping resulted in limited suppression of the superconducting transition temperature and an increase in the normal-state resistivity. Magnetic and levitation characterizations showed that the sample containing 15 wt% $C_{15}H_{12}O_2$ exhibited the highest critical current density at 20 K, optimized pinning force, and stable levitation behavior. The findings reveal that $C_{15}H_{12}O_2$ addition offers a practical approach for adjusting the condensation–pinning equilibrium in SPS-produced MgB_2 bulk superconductors, and that such organic additive has significant potential in the development of high-performance MgB_2 bulk materials.

Author contributions

Asli Asiye Agil: Investigation, Methodology, Writing.

Funding

Open access funding provided by the Scientific and Technological Research Council of Türkiye (TÜBİTAK).

Data availability

Data will be made available on request.

Declarations

Competing interests The authors declare no competing interests.

Open Access This article is licensed under a Creative Commons Attribution 4.0 International License, which permits use, sharing, adaptation, distribution and reproduction in any medium or format, as long as you give appropriate credit to the original author(s) and the source, provide a link to the Creative Commons licence, and indicate if changes were made. The images or other third party material in this article are included in the article's Creative Commons licence, unless indicated otherwise in a credit line to the material. If material is not included in the article's Creative Commons licence and your intended use is not permitted by statutory regulation or exceeds the permitted use, you will need to obtain permission directly from the copyright holder. To view a copy of this licence, visit http://creativecommons.org/licenses/by/4.0/.

References

1. J. Nagamatsu, N. Nakagawa, T. Muranaka, Y. Zenitani, J. Akimitsu, Superconductivity at 39 K in magnesium diboride. Nature **410**, 63–64 (2001). https://doi.org/10.1038/35065039
2. J.H. Durrell, C.E.J. Dancer, A. Dennis, Y. Shi, Z. Xu, A.M. Campbell, N. Hari Babu, R.I. Todd, C.R.M. Grovenor, D.A. Cardwell, A trapped field of >3 T in bulk MgB_2 fabricated by uniaxial hot pressing. Supercond. Sci. Technol. **25**, 112002 (2012). https://doi.org/10.1088/0953-2048/25/11/112002
3. A.G. Bhagurkar, A. Yamamoto, N. Hari Babu, J.H. Durrell, A.R. Dennis, D.A. Cardwell, Synthesis of dense bulk MgB_2 by an infiltration and growth process. Supercond. Sci. Technol. **28**, 015012 (2015). https://doi.org/10.1088/0953-2048/28/1/015012
4. Y. Xing, P. Bernstein, M. Miryala, J.G. Noudem, High critical current density of nanostructured MgB_2 bulk superconductor densified by spark plasma sintering. Nanomaterials **12**(15), 2583 (2022). https://doi.org/10.3390/nano12152583
5. A.G. Bhagurkar, A. Yamamoto, L. Wang, M. Xia, A.R. Dennis, J.H. Durrell, T.A. Aljohani, N.H. Babu, D.A. Cardwell, High trapped fields in C-doped MgB_2 bulk superconductors fabricated by infiltration and growth process. Sci. Rep. **8**, 13320 (2018). https://doi.org/10.1038/s41598-018-31416-3
6. K. Yokoyama, T. Oka, K. Berger, R. Dorget, M. Koblischka, M. Grigoroscuta, M. Burdusel, D. Batalu, G. Aldica, P. Badica, N. Sakai, M. Muralidhar, M. Murakami, Investigation of flux jumps during pulsed field magnetization in graphene-added MgB_2 bulks. J. Phys. Conf. Ser. **1559**, 012080 (2020). https://doi.org/10.1088/1742-6596/1559/1/012080
7. J. Zou, M.D. Ainslie, H. Fujishiro, A.G. Bhagurkar, T. Naito, N. Hari Babu, J.-F. Fagnard, P. Vanderbemden, A. Yamamoto, Numerical modelling and comparison of MgB_2 bulks fabricated by HIP and infiltration growth. Supercond. Sci. Technol. **28**, 075009 (2015). https://doi.org/10.1088/0953-2048/28/7/075009
8. J.L. Dadiel, S.P.K. Naik, P. Pęczkowski, J. Sugiyama, H. Ogino, N. Sakai, Y. Kazuya, T. Warski, A. Wojcik, T. Oka, M. Murakami, Synthesis of dense MgB_2 superconductor via in situ and ex situ spark plasma sintering method. Materials **14**(23), 7395 (2021). https://doi.org/10.3390/ma14237395
9. D. Batalu, G. Aldica, S. Popa, A. Kuncser, V. Mihalache, P. Badica, GeO_2-added MgB_2 superconductor obtained by spark plasma sintering. Solid State Sci. **48**, 23–30 (2015). https://doi.org/10.1016/j.solidstatesciences.2015.06.013
10. S.M. Kazakov, R. Puzniak, K. Rogacki, A.V. Mironov, N.D. Zhigadlo, J. Jun, C. Soltmann, B. Batlogg, J. Karpinski, Carbon substitution in MgB_2 single crystals: structural and superconducting properties. Phys. Rev. B **71**, 024533 (2005). https://doi.org/10.1103/PhysRevB.71.024533
11. Y. Zhang, S.H. Zhou, C. Lu, K. Konstantinov, S.X. Dou, The effect of carbon doping on the upper critical field (H_{c2})

and resistivity of MgB_2 by using sucrose ($C_{12}H_{22}O_{11}$) as the carbon source. Supercond. Sci. Technol. **22**, 015025 (2009). https://doi.org/10.1088/0953-2048/22/1/015025

12. D. Matera, M. Bonura, R. Černý, S. McKeown Walker, F. Buta, D. LeBoeuf, X. Chaud, E. Giannini, C. Senatore, High-field superconductivity in C-doped MgB_2 bulk samples prepared by a rapid synthesis route. Sci. Rep. **10**, 17656 (2020). https://doi.org/10.1038/s41598-020-74300-9
13. S.O. Olatunji, T. Owolabi, Extreme learning machine approach to modeling the superconducting critical temperature of doped MgB_2 superconductor. Crystals **12**, 228 (2022). https://doi.org/10.3390/cryst12020228
14. E.J. Corey, M. Chaykovsky, Dimethyloxosulfonium Methylide ($(CH_3)_2SOCH_2$) and Dimethylsulfonium Methylide ($(CH_3)_2SCH_2$). Formation and Application to Organic Synthesis. J. Am. Chem. Soc. **87**, 1353–1364 (1965). https://doi.org/10.1021/ja01084a034
15. H. Ağıl, A.A. Agil, S.B. Güner, E. Ayas, Investigation of MgB_2 bulk superconductors synthesized by in situ spark plasma sintering at different temperatures. Mater. Chem. Phys. **306**, 128010 (2023). https://doi.org/10.1016/j.matchemphys.2023.128010
16. P. Badica, G. Aldica, M.A. Grigoroscuta, M. Burdusel, I. Pasuk, D. Batalu, K. Berger, A. Koblischka-Veneva, M.R. Koblischka, Reproducibility of small $Ge_2C_6H_{10}O_7$-added MgB_2 bulks fabricated by ex situ Spark Plasma Sintering used in compound bulk magnets with a trapped magnetic field above 5 T. Sci. Rep. **10**, 10538 (2020). https://doi.org/10.1038/s41598-020-67463-y
17. D.K. Kang, D.W. Kim, S.H. Choi, C.J. Kim, I.S. Ahn, Phase formation of MgB_2 superconducting materials fabricated by spark plasma sintering. Met. Mater. Int. **15**, 15–19 (2009). https://doi.org/10.1007/s12540-009-0015-x
18. Z. Zhang, J. MacManus-Driscoll, H. Suo, Q. Wang, Review of synthesis of high volumetric density, low gravimetric density MgB_2 bulk for potential magnetic field applications. Superconductivity **3**, 100015 (2022). https://doi.org/10.1016/j.supcon.2022.100015
19. M. Prakasam, F. Balima, J. Noudem, A. Largeteau, Dense MgB_2 ceramics by ultrahigh pressure field-assisted sintering. Ceramics **3**, 521–532 (2020). https://doi.org/10.3390/ceramics3040042
20. Y. Zhao, Y. Feng, C.H. Cheng, L. Zhou, Y. Wu, T. Machi, Y. Fudamoto, N. Koshizuka, M. Murakami, High critical current density of MgB_2 bulk superconductor doped with Ti and sintered at ambient pressure. Appl. Phys. Lett. **79**, 1154–1156 (2001). https://doi.org/10.1063/1.1396629
21. S.S. Arvapalli, M. Miryala, M. Jirsa, N. Sakai, M. Murakami, Pinning behavior in bulk MgB_2 prepared using boron powder refined via high-energy ultra-sonication. J. Supercond. Nov. Magn. **34**, 1297–1301 (2021). https://doi.org/10.1007/s10948-021-05885-z
22. Q. Wang, L. Li, Y. Zhao, H. Zhang, Y. Zhang, The effects of sintering temperature on superconductivity of MgB_2 prepared by hot pressing. Int. J. Mod. Phys. B **34**(04), 2050012 (2020). https://doi.org/10.1142/S0217979220500125
23. A.T. Findikoglu, A. Serquis, L. Civale, X.Z. Liao, Y.T. Zhu, M.E. Hawley, F.M. Mueller, V.F. Nesterenko, Y. Gu, Microwave performance of high-density bulk MgB_2. Appl. Phys. Lett. **83**, 108–110 (2003). https://doi.org/10.1063/1.1590739
24. A. Sklyarova, L. Presmanes, V. Baylac, G. Chevallier, C. Estournès, B. Duployer, J. Noudem, P. Bernstein, P. Tailhades, Y. Thimont, Processing of bulk MgB_2 superconductors by coupling laser powder bed fusion and spark plasma sintering techniques. Materials **18**, 2367 (2025). https://doi.org/10.3390/ma18102367
25. M. Rafieazad, Ö. Balcı, S. Acar, M. Somer, Review on magnesium diboride (MgB_2) as excellent superconductor: effects of the production techniques on the superconducting properties. Journal of Boron **2**(2), 87–96 (2017)
26. V. Grinenko, E.P. Krasnoperov, V.A. Stoliarov, A.A. Bush, B.P. Mikhajlov, Superconductivity in porous MgB_2. Solid State Commun. **138**(9), 461–465 (2006). https://doi.org/10.1016/j.ssc.2006.03.036
27. G.A.B. Matthews, J. Liu, C.R.M. Grovenor, P.S. Grant, S. Speller, Design and characterisation of ex situ bulk MgB_2 superconductors containing a nano-scale dispersion of artificial pinning centres. Supercond. Sci. Technol. **33**, 034006 (2020). https://doi.org/10.1088/1361-6668/ab6959
28. X. Xu, W. Li, X. Wang, S.X. Dou, Superconducting Properties of Graphene Doped Magnesium Diboride, Applications of High-T_c Superconductivity, ed by A.M. Luiz (IntechOpen, Rijeka, 2011), https://doi.org/10.5772/17117
29. S. Lee, T. Masui, A. Yamamoto, H. Uchiyama, S. Tajima, Carbon-substituted MgB_2 single crystals. Physica C **397**(1–2), 7–13 (2003). https://doi.org/10.1016/S0921-4534(03)01296-6
30. T. Takenobu, T. Ito, D.H. Chi, K. Prassides, Y. Iwasa, Intralayer carbon substitution in the MgB_2 superconductor. Phys. Rev. B **64**, 134513 (2001). https://doi.org/10.1103/PhysRevB.64.134513
31. M. Shahbazi, A.S. Pannu, J. Alarco, P. Sonar, I. Mackinnon, Impact of hair-derived carbon substitution on structural and superconducting properties of MgB_2. AIP Adv. **13**, 125318 (2023). https://doi.org/10.1063/5.0174642
32. E. Yanmaz, C. Castillo-Berrio, Ü. Alkan, A.T. Ülgen, F. Karaboğa, O. Enis, D. Odabaşı Cingi, P. Alcan, İ Saraçoğlu, Bulk Mg_xB_2 superconductor production by excess Mg and

hot press methods and their properties. Journal of Boron **2**(1), 43–48 (2017)
33. A.G. Bhagurkar, A. Yamamoto, A.R. Dennis, J.H. Durrell, T.A. Aljohani, H.B. Nadendla, D.A. Cardwell, Microstructural evolution in infiltration-growth processed MgB_2 bulk superconductors. J. Am. Ceram. Soc. **100**, 2451–2460 (2017). https://doi.org/10.1111/jace.14792
34. T.A. Prikhna, A.P. Shapovalov, G.E. Grechnev, V.G. Boutko, A.A. Gusev, A.V. Kozyrev, M.A. Belogolovskiy, V.E. Moshchil, V.B. Sverdun, Formation of nanostructure in magnesium diboride based materials with high superconducting characteristics. Low Temp. Phys. **42**, 380–394 (2016). https://doi.org/10.1063/1.4952985
35. S.S. Arvapalli, M. Muralidhar, M. Murakami, High-performance bulk MgB_2 superconductor using amorphous nanoboron. J. Supercond. Nov. Magn. **32**, 1891–1895 (2019). https://doi.org/10.1007/s10948-018-4919-x
36. T.A. Prikhna, W. Gawalek, W. Goldacker, Y.M. Savchuk, J. Noudem, A. Soldatov, M. Eisterer, H.W. Weber, V. Sokolovsky, M. Serga, S.N. Dub, M. Wendt, S. You, N.V. Sergienko, V.E. Moshchil, V.N. Tkach, J. Dellith, F. Karau, M. Tomsic, C. Shmidt, I.P. Fesenko, T. Habisreuther, D. Litzkendorf, V. Meerovich, V.B. Sverdun, High-pressure synthesized nanostructural MgB_2 materials with high performance of superconductivity, suitable for fault current limitation and other applications. IEEE Trans. Appl. Supercond. **21**(3), 2694–2697 (2011). https://doi.org/10.1109/TASC.2010.2096494
37. M. Miryala, K. Kitamoto, S.S. Arvapalli, D. Das, M. Jirsa, M. Murakami, S.R.R. Mamidanna, Enhancing critical current density of bulk MgB_2 via nano-scale boron and Dy_2O_3 doping. Adv. Eng. Mater. **24**, 2200487 (2022). https://doi.org/10.1002/adem.202200487
38. T. Prikhna, V. Sokolovsky, V. Moshchil, Bulk MgB_2 superconducting materials: technology, properties, and applications. Materials **17**, 2787 (2024). https://doi.org/10.3390/ma17112787
39. D. Gajda, A. Morawski, A.J. Zaleski, M. Akdoğan, H. Yetiş, F. Karaboğa, T. Cetner, I. Belenli, The influence of HIP process on critical parameters of MgB_2/Fe wires with big boron grains and without barriers. J. Alloys Compd. **687**, 616–622 (2016). https://doi.org/10.1016/j.jallcom.2016.06.095
40. Y. Shimada, S. Hata, K.-I. Ikeda, H. Nakashima, S. Matsumura, H. Tanaka, A. Yamamoto, J.-I. Shimoyama, K. Kishio, Microstructural connectivity in sintered ex-situ MgB_2 bulk superconductors. J. Alloys Compd. **656**, 172–180 (2016). https://doi.org/10.1016/j.jallcom.2015.09.253
41. C.U. Jung, H.-J. Kim, M.-S. Park, M.-S. Kim, J.Y. Kim, Z. Du, S.-I. Lee, K.H. Kim, J.B. Betts, M. Jaime, A.H. Lacerda, G.S. Boebinger, Effects of unreacted Mg impurities on the transport properties of MgB_2. Phys. C Supercond. **377**(1–2), 21–25 (2002). https://doi.org/10.1016/S0921-4534(02)01334-5
42. A. Vajpayee, V.P.S. Awana, G.L. Bhalla, P.A. Bhobe, A.K. Nigam, H. Kishan, Superconducting properties of adipic-acid-doped bulk MgB_2 superconductor. Supercond. Sci. Technol. **22**, 015016 (2009). https://doi.org/10.1088/0953-2048/22/1/015016
43. C.P. Bean, Magnetization of hard superconductors. Phys. Rev. Lett. **8**, 250 (1962). https://doi.org/10.1103/PhysRevLett.8.250
44. C.P. Bean, Magnetization of high-field superconductors. Rev. Mod. Phys. **36**, 31 (1964). https://doi.org/10.1103/RevModPhys.36.31
45. E.M. Gyorgy, R.B. van Dover, K.A. Jackson, L.F. Schneemeyer, J.V. Waszczak, Anisotropic critical currents in $Ba_2YCu_3O_7$ analyzed using an extended Bean model. Appl. Phys. Lett. **55**, 283–285 (1989). https://doi.org/10.1063/1.102387
46. E.J. Kramer, Scaling laws for flux pinning in hard superconductors. J. Appl. Phys. **44**, 1360–1370 (1973). https://doi.org/10.1063/1.1662353
47. V. Sandu, A.M. Ionescu, G. Aldica, M.A. Grigoroscuta, M. Burdusel, P. Badica, On the pinning force in high density MgB_2 samples. Sci. Rep. **11**, 5951 (2021). https://doi.org/10.1038/s41598-021-85209-2
48. S.B. Güner, B. Savaşkan, K. Öztürk, Ş Çelik, C. Aksoy, F. Karaboğa, E. Taylan Koparan, E. Yanmaz, Investigation on superconducting and magnetic levitation force behaviour of excess Mg doped-bulk MgB_2 superconductors. Cryogenics **101**, 131–136 (2019). https://doi.org/10.1016/j.cryogenics.2019.05.002
49. J.G. Noudem, P. Bernstein, L. Dupont, F.G.R. Martin, G.G. Sotelo, D.H.N. Dias, R.M. AndradeMuralidhar Jr., M. Murakami, Spark plasma sintering of bulk MgB_2 and levitation force measurements. Supercond. Sci. Technol. **33**, 024001 (2020). https://doi.org/10.1088/1361-6668/ab5f3e
50. Ş Çelik, Design of magnetic levitation force measurement system at any low temperatures from 20 K to room temperature. J. Alloys Compd. **662**, 546–556 (2016). https://doi.org/10.1016/j.jallcom.2015.11.230
51. D. Tripathi, A. Bhatnagar, S. Raj, D.K. Rai, T.K. Dey, Levitation force of graphene added bulk MgB_2 superconductor.

Cryogenics **118**, 103343 (2021). https://doi.org/10.1016/j.cryogenics.2021.103343

Publisher's Note Springer Nature remains neutral with regard to jurisdictional claims in published maps and institutional affiliations.